High Thermoelectric Performance of p-Type SnTe via a Synergistic Band Engineering and Nanostructuring Approach

Gangjian Tan,[†] Li-Dong Zhao,[†] Fengyuan Shi,[‡] Jeff W. Doak,[‡] Shih-Han Lo,[‡] Hui Sun,[§] Chris Wolverton,[‡] Vinayak P. Dravid,[‡] Ctirad Uher,[§] and Mercouri G. Kanatzidis*,[†,∥]

[†]Department of Chemistry and [‡]Department of Materials Science and Engineering, Northwestern University, Evanston, Illinois 60208, United States

[§]Department of Physics, University of Michigan, Ann Arbor, Michigan 48109, United States

[∥]Materials Science Division, Argonne National Laboratory, Argonne, Illinois 60439, United States

S *Supporting Information*

ABSTRACT: SnTe is a potentially attractive thermoelectric because it is the lead-free rock-salt analogue of PbTe. However, SnTe is a poor thermoelectric material because of its high hole concentration arising from inherent Sn vacancies in the lattice and its very high electrical and thermal conductivity. In this study, we demonstrate that SnTe-based materials can be controlled to become excellent thermoelectrics for power generation via the successful application of several key concepts that obviate the well-known disadvantages of SnTe. First, we show that Sn self-compensation can effectively reduce the Sn vacancies and decrease the hole carrier density. For example, a 3 mol % self-compensation of Sn results in a 50% improvement in the figure of merit ZT. In addition, we reveal that Cd, nominally isoelectronic with Sn, favorably impacts the electronic band structure by (a) diminishing the energy separation between the light-hole and heavy-hole valence bands in the material, leading to an enhanced Seebeck coefficient, and (b) enlarging the energy band gap. Thus, alloying with Cd atoms enables a form of valence band engineering that improves the high-temperature thermoelectric performance, where p-type samples of $SnCd_{0.03}Te$ exhibit ZT values of ~0.96 at 823 K, a 60% improvement over the Cd-free sample. Finally, we introduce endotaxial CdS or ZnS nanoscale precipitates that reduce the lattice thermal conductivity of $SnCd_{0.03}Te$ with no effect on the power factor. We report that $SnCd_{0.03}Te$ that are endotaxially nanostructured with CdS and ZnS have a maximum ZTs of ~1.3 and ~1.1 at 873 K, respectively. Therefore, SnTe-based materials could be ideal alternatives for p-type lead chalcogenides for high temperature thermoelectric power generation.
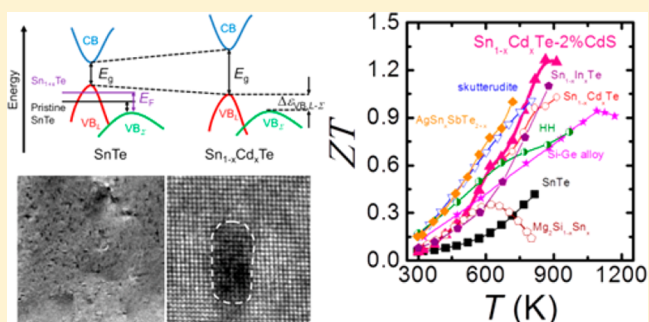
INTRODUCTION

Clean and reliable energy conversion technologies are highly sought after due to increasing global concerns for energy efficiency and conservation. Thermoelectric materials can be used to directly convert waste heat into electrical power and have attracted significant attention for electricity generation from solar energy and waste heat recovery.[1−9] The conversion efficiency is governed by the thermoelectric figure of merit (ZT) defined as $ZT = S^2\sigma T/\kappa$, where S, σ, T, and κ denote the Seebeck coefficient, electrical conductivity, absolute temperature, and thermal conductivity, respectively.[10−12] The most commonly pursued approaches to enable high ZT include the manipulation of the density of states by band engineering for high power factors ($S^2\sigma$) (such as the introduction of resonant impurity levels near the Fermi level,[13−16] band convergence/degeneracy,[17−19] etc.), or blocking of phonon propagation through alloying and nanostructuring to minimize the thermal conductivity.[7,20−34]

Nanostructured lead chalcogenides PbQ (Q = Te, Se, S) and their alloys have been demonstrated to be efficient thermoelectric materials in the temperature range of 600−900 K.[19,28−30,35] PbTe-based materials have the highest reported performance with the maximum ZT values reaching ~2.2 for the p-type $Pb_{1−x}Na_xTe$-SrTe system.[33] For Te-free members including PbSe and PbS, thermoelectric performance can be enhanced through a synergistic band structure engineering and compositionally alloyed nanostructuring approach, with ZT values increased to 1.6 and 1.3, respectively.[30,35] Recently, however, a desire for Pb-free materials has emerged due to a perceived toxicity of PbQ.

SnTe, a lead-free compound which is isostructural with rock-salt PbQ, has seldom been regarded as a promising thermoelectric material because of its low ZT. This low efficiency is attributed mainly to the poor Seebeck coefficient and high

thermal conductivity arising from its ultrahigh hole density ($>10^{21}$ cm^{-3}) caused by the intrinsically very large number of Sn lattice vacancies.[36,37] (Despite this large number of vacancies and the fact that the compound is inherently off-stoichiometric, the material is still often referred to as SnTe.) Electronic structure calculations show that SnTe has a similar band structure to the lead chalcogenides, which suggests that it has potential as a good thermoelectric material.[38−40] The valence and conduction band edges of SnTe are located at the L point of the Brillouin zone and are separated by a very small energy gap of 0.18 eV at room temperature.[41,42] Lying energetically below the valence band is a flatter, so-called heavy-hole band which lies along Σ. In SnTe the energy difference between the light-hole band at L and the heavy-hole band at Σ is around 0.3−0.4 eV.[26,38,40] This energy difference is much larger than in the case of PbTe (0.17 eV) or PbSe (0.24 eV),[43] thus preventing the heavier hole mass in SnTe from significantly contributing to the Seebeck coefficient. Moreover, the very small band gap of SnTe is not helpful in retaining a high thermoelectric performance at elevated temperature because of bipolar diffusion.

In this contribution, we report the realization of high thermoelectric performance in SnTe-based materials through three separate synergistic strategies, namely, (a) suppression of excess hole carrier densities, (b) successful band structure engineering to further increase the power factor, and (c) nanostructuring to reduce lattice thermal conductivity. First, we demonstrate that through Sn self-compensation we can efficiently decrease the intrinsically high hole concentration of SnTe to greatly improve the thermoelectric performance. For example, the 3 mol % Sn self-compensated sample (Sn$_{1.03}$Te) has a ZT value of ∼0.6 at 823 K, which is 50% improvement over the "pristine" SnTe. Second, we show that by alloying Cd at Sn lattice sites on the Sn-rich Sn$_{1+x}$Te system, a further decrease of the hole concentration is achieved to a nearly optimal level of ∼5 × 10^{19} cm^{-3}. More importantly, we show that the introduction of Cd significantly modifies the electronic band structure of SnTe by enlarging the band gap, which is important for the high temperature thermoelectric performance, and decreases the energy separation between the light-hole and heavy-hole maxima, from 0.35 eV in pristine SnTe to 0.12 eV for 3 mol % Cd alloyed sample. The resultant band convergence markedly improves the electronic density of states, thereby enhancing the Seebeck coefficients over a wide temperature range. From the Cd alloying alone a maximum ZT value of ∼0.96 at 823 K is observed. Third, we successfully introduce CdS/ZnS nanoscale precipitates into the matrix. These second phase precipitates exhibit three symmetry related variants with coherent or semicoherent interfaces of well-defined orientational relationship with the SnTe matrix. These exert little influence on the hole charge transport but seem effective in scattering the heat-carrying phonons to reduce the lattice thermal conductivity. As a consequence, these p-type nanostructured SnCd$_{0.03}$Te samples obtain a maximum ZT of ∼1.3 and ∼1.1 at 873 K for CdS and ZnS, respectively. These results introduce a new generation of lead-free SnTe-based materials that rise to the level of excellent p-type thermo-electrics.

■ EXPERIMENTAL PROCEDURES

Synthesis. Reagent chemicals were used as obtained: Sn chunk (99.9999%, American Elements, US), Cd shot (99.99%,

Alfa, US), Zn shot (99.99%, Baker, US), Te shot (99.999%, 5N Plus, Canada), and S chunk (99.999%, Inc., Canada).

Synthesis of Starting Materials. SnTe-based compounds with Sn self-compensation, Cd-doping, and CdS/ZnS nanostructuring were synthesized by a melting combined with spark plasma sintering (SPS) technique as described below. High-purity elemental Sn, Cd, Te, Zn, and S were weighed according to the nominal compositions of Sn$_{1+x}$Te (x = 0, 0.01, 0.02, 0.03, 0.04, 0.06, 0.08, and 0.10), Sn$_{1.03−x}$Cd$_x$Te (x = 0.01, 0.02, 0.03, 0.04, 0.05, and 0.06), and SnCd$_{0.03}$Te-x mol % CdS/ZnS (x = 1, 2, 3, 4, and 5), and then put inside 13-mm-diameter fused quartz tubes. The tubes were then evacuated to a pressure of ∼10^{-4} Torr, flame-sealed, and melted in computer controlled furnaces. For a typical experiment the following amounts were used: Sn (3.7600 g, 31.6742 mmol), Cd (0.1780 g, 1.584 mmol), Te (4.0416 g, 31.6742 mmol), and S (0.0204 g, 0.6335 mmol) were used to prepare 8 g of SnCd$_{0.03}$Te-2 mol % CdS. The heating profiles differed for different compositions. For Sn$_{1+x}$Te, the samples were slowly heated to 1123 K in 10 h, soaked at this temperature for 6 h, and subsequently cooled to room temperature by turning off the furnace. For Sn$_{1.03−x}$Cd$_x$Te, the samples were slowly heated to 1273 K in 10 h, soaked at this temperature for 6 h and subsequently quenched in ice water. For SnCd$_{0.03}$Te-x mol % CdS/ZnS, the samples were slowly heated to 723 K in 10 h, soaked there for 6 h, then to 1423 K in 7 h, soaked at this temperature for 10 h, and subsequently quenched in ice water. The resultant ingots were crushed into fine powders and then densified by SPS method (SPS-211LX, Fuji Electronic Industrial Co., Ltd.). To prepare for SPS processing, the melt grown ingots were ground to a powder using an agate mortar and pestle to reduce the grain size to smaller than 1 mm in diameter and then further ground by a mechanical mortar and pestle to reduce the grains to less than 4 μm in diameter. These powders were then densified at 723 K for 5 min in a 12.7-mm-diameter graphite die under an axial compressive stress of 40 MPa in vacuum. Highly dense (>95% of theoretical density) disk-shaped pellets with dimensions of 12.7 mm diameter and 8 mm thickness were obtained.

Physical Characterization. *Electrical Properties.* The obtained SPS processed pellets were cut into bars with dimensions 12 mm × 3 mm × 3 mm that were used for simultaneous measurement of the Seebeck coefficient and the electrical conductivity using an Ulvac Riko ZEM-3 instrument under a low-pressure helium atmosphere from room temperature to 823 or 923 K. The uncertainty of the Seebeck coefficient and electrical conductivity measurements is 5%.

Thermal Conductivity. High density SPS processed pellets were cut and polished into a squared shape of 6 × 6 × 2 mm^3 for thermal diffusivity measurements. The samples were coated with a thin layer of graphite to minimize errors from the emissivity of the material. The thermal conductivity was calculated from $\kappa = D \cdot C_p \cdot d$, where the thermal diffusivity coefficient (D) was measured using the laser flash diffusivity method in a Netzsch LFA457, the specific heat capacity (C_p) was indirectly derived using a representative sample (Pyroceram 9606) in the range 300−923 K, and the density (d) was determined using the dimensions and mass of the sample, which was then reconfirmed using gas pycnometer (Micromeritics AccuPyc1340) measurements. The thermal diffusivity data were analyzed using a Cowan model with pulse correction, and heating and cooling cycles give reproducible values for each sample (see Supporting Information). Thermal diffusivities

obtained for different slices from the same pellet are very similar, suggesting the good homogeneity of the samples. The uncertainty of the thermal conductivity is estimated to be within 8%, considering the uncertainties for D, C_p, and d. The thermal diffusion and the heat capacity data for all samples can be found in the Supporting Information. The combined uncertainty for all measurements involved in the calculation of ZT is less than 15%. No directional anisotropy effects were observed in the charge transport properties.

Hall Measurements. The room temperature Hall coefficients were measured on a home-built system in magnetic fields ranging from 0 to 1.25 T, utilizing simple four-contact Hall-bar geometry, in both negative and positive polarity to eliminate Joule resistive errors. The high temperature Hall measurements for several selected samples were performed on a homemade apparatus (University of Michigan) which provides a working range from 300 to ~873 K. The samples were press mounted and protected with argon gas to avoid possible oxidization at high temperature. The Hall resistance was monitored with a Linear Research AC Resistance Bridge (LR-700), with constant magnetic fields of ±1 T applied by using an Oxford Superconducting magnet.

Electron Microscopy and X-ray Diffraction. Scanning transmission and transmission electron microscopy (TEM) investigations were carried out in a JEOL 2100F microscope operated at 200 kV. The thin TEM specimens were prepared by conventional methods, including cutting, grinding, dimpling, tripod, with minimal duration of Ar-ion milling with a liquid N_2 cooling stage.[44] Samples pulverized with an agate mortar were used for powder X-ray diffraction (XRD). The powder diffraction patterns were obtained with Cu K$_a$ (λ = 1.5418 Å) radiation in a reflection geometry on an Inel diffractometer operating at 40 kV and 20 mA and equipped with a position-sensitive detector.

Band Structure Calculations. Density functional theory (DFT)[45,46] calculations of pristine, stoichiometric SnTe and Cd-doped SnTe were carried out using the Vienna *ab initio* Simulation Package (VASP),[47] using projector-augmented wave (PAW) potentials[48] making use of the exchange-correlation functional of Perdew, Burke, and Erzenhoff (PBE).[49] Potentials for Sn, Cd, and Te contain as valence electrons the $4d^{10}5s^25p^2$, $4d^{10}5s^2$, and $5s^25p^4$ electrons, respectively. Pure and Cd-doped SnTe supercells were fully relaxed according to the relaxation scheme of the Open Quantum Materials Database (OQMD).[50] Final total energies were calculated using cutoff energies of 520 eV, 5 × 5 × 5 Γ-centered *k*-point meshes, and tetrahedral *k*-point integration. Band structure calculations were performed with 520 eV cutoff energies and 20 *k*-points each along the lines from L to Γ and from Γ to K in the rock-salt Brillouin zone.

Structural relaxations and band structure calculations were performed for 54-atom supercells of the SnTe rock-salt primitive unit cell containing either 0, 1, or 2 Cd atoms substituted for Sn atoms. For the case of 2 substitutional Cd atoms, there were multiple Cd−Cd arrangements which could be created in the supercell. We calculated Cd−Cd defect pairs in the first to third nearest neighbor positions (4.5 Å to 7.8 Å Cd−Cd distance) on the Sn sublattice, and calculated relaxations and band structures for each of the configurations.

Electron eigenvalues of the defect band structures were aligned to the electron eigenvalues of the pristine SnTe band structure through an electrostatic potential alignment procedure.[51] We calculated the average electrostatic potential around each atom in the pristine SnTe supercell, as well as in the defect

supercells. We then averaged the difference in electrostatic potential between atoms in defect supercell and atoms in the pristine SnTe supercell, over all atoms lying outside a radius of one-half the periodic image distance, centered at the Cd defect for the case of one Cd substitution, or centered in between two Cd defects for the $Sn_{25}Cd_2Te_{27}$ defect supercells. Subtracting this averaged electrostatic potential difference from the electron eigenvalues of the defect supercell puts the band structure of the defect supercell on the same energy scale as the pristine SnTe supercell, allowing an accurate comparison of band structures.

RESULTS AND DISCUSSION

SnTe is a highly degenerate p-type semiconductor with large hole concentration ($\sim 10^{21}$ cm^{-3}) ascribed to the intrinsic Sn deficiency, making it a poor thermoelectric.[40] To obtain improved thermoelectric performance, it is necessary to decrease the hole concentration to a proper level, i.e., on the order of 10^{19} cm^{-3}. Electron donor doping could help accomplish this, but the challenge is that the typical elements that are efficient electron donors in lead chalcogenides (e.g., Sb, Bi, Br, I) fail for SnTe,[52] and in some cases, apparent electron donors, actually act as electron acceptors, such as indium.[26] This anomalous behavior is related to the fact that each Sn-vacancy is substantially a two-electron acceptor, but most additives donate only one electron (e.g., In, Bi, and Sb) to the system. Therefore, when doped into SnTe, these additives can act as one-electron acceptors.[26] In this regard, we hypothesized that Sn self-compensation could be an effective way of neutralizing the overly high hole concentration of SnTe. In this discussion, first we concentrate on the effects of Sn compensation on the thermoelectric transport properties of SnTe, we then present in detail the valence band modifying effects of Cd alloying, and finally we discuss the results of incorporating CdS/ZnS nanostructures in SnTe as thermal conductivity reducing second phases.

1. Sn Self-Compensation. Figure 1a depicts the powder XRD patterns of sintered samples of $Sn_{1+x}Te$ (x = 0, 0.01, 0.02, 0.03, 0.04, 0.06, 0.08, and 0.10). The main Bragg reflections of all samples correspond well to the rock-salt structure, indicating SnTe as the major phase. For the samples with $x \leq 0.04$, no impurity phases were observed within our detection limit, while for the samples with $x \geq 0.06$, two additional peaks were
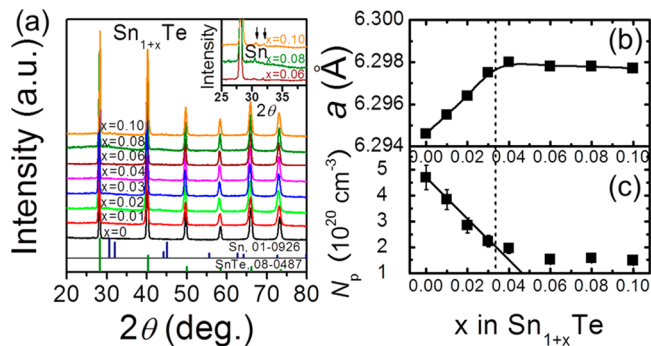

Figure 1. (a) Powder XRD patterns of $Sn_{1+x}Te$ (x = 0−0.1) samples, (b) lattice parameters, and (c) carrier density as a function of x at room temperature. Inset of (a): enlarged powder XRD pattern ranged from 25° to 39° (2θ deg). At the bottom of (a) standard diffraction patterns of SnTe (JCPDS Card 08−0487) and Sn (JCPDS Card 01−0926).
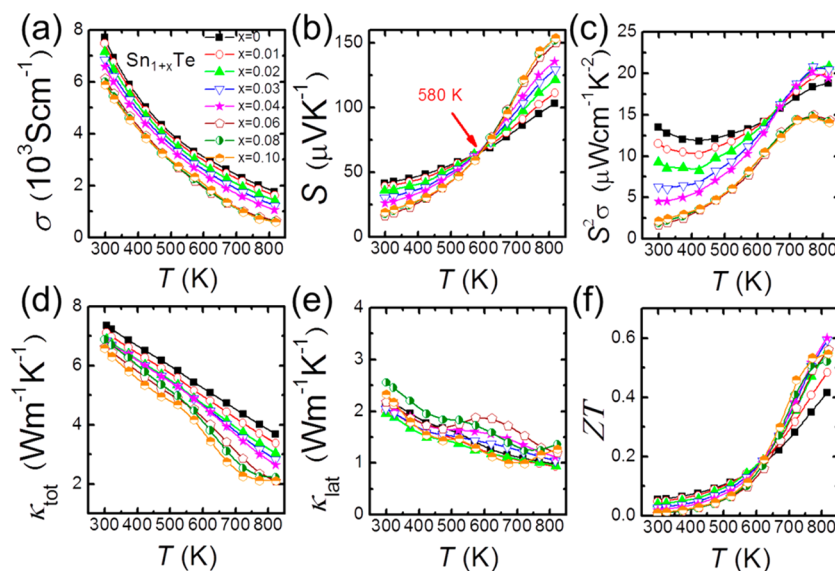
Figure 2. Thermoelectric properties as a function of temperature for SnTe with different Sn content: (a) electrical conductivity; (b) Seebeck coefficient; (c) power factor; (d) total thermal conductivity; (e) lattice thermal conductivity; (f) ZT.

observed ($2\theta = \sim30.7°$ and $\sim32.1°$) that can be assigned to Sn; see inset of Figure 1a. The lattice parameter as a function of x increases gradually with increasing Sn content and then saturates at $x > 0.03$, which suggests that the added Sn can successfully fill into the Sn vacancies until $x = 0.03$ (Figure 1b). Figure 1c shows the room temperature Hall carrier concentrations (N_p) as a function of x for $Sn_{1+x}Te$. The $x = 0$ sample (pristine SnTe) has a high hole density of 4.7×10^{20} cm^{-3}, but with increasing Sn content, the hole concentration clearly decreases. The solid line in Figure 1c shows the hole concentrations with x calculated assuming each compensating Sn atom donates two electrons. The Hall carrier concentration shows good agreement with the expected results except for the samples with $x > 0.03$. This confirms the two-electron acceptor nature of each Sn vacancy and indicates that the limit for Sn-compensation in SnTe is ~0.03.

Figure 2 shows the temperature dependent thermoelectric properties for the $Sn_{1+x}Te$ compounds with different Sn content. The sample with $x = 0$ has a very high electrical conductivity of ~7800 S/cm at room temperature, consistent with its large hole density. With increasing x, the room temperature electrical conductivity systematically decreases and then remains almost unchanged at ~6000 S/cm when $x \geq 0.06$. This behavior is consistent with the trend of the Hall carrier concentration.

The Seebeck coefficients, as shown in Figure 2b, are positive for all $Sn_{1+x}Te$ samples, which is consistent with the sign of Hall carrier concentration (Figure 1c). The $x = 0$ sample possesses a low Seebeck coefficient of ~41 μV/K at room temperature because of its high hole concentration as mentioned above. Interestingly, the room temperature Seebeck coefficient decreases gradually with increasing x despite the reduced hole concentration, which is opposite from the usual behavior expected for a p-type semiconductor. This anomalous variation in Seebeck coefficient is related to the unique character of the two nondegenerate valence bands (at the L and Σ points of the Brillouin zone) of SnTe.[38,40] In the two-valence band case, the total Seebeck coefficient is given by[17]

$$S = \frac{S_{lh}\sigma_{lh} + S_{hh}\sigma_{hh}}{\sigma_{lh} + \sigma_{hh}} \tag{1}$$

In eq 1, the S_{lh} and S_{hh} denote the Seebeck coefficient of the light-hole band and heavy-hole band respectively, while σ_{lh} abd σ_{hh} represent the electrical conductivity from light-hole band and heavy-hole band contribution, respectively. Because of the very high hole concentration in pristine SnTe, the Fermi level is lower in energy and closer to the heavy-hole band.[53] Thus, the Seebeck coefficient is affected by hole carriers excited from the heavy-hole band at high temperature.[54] With decreasing hole concentration, however, in $Sn_{1+x}Te$ the Fermi level rises and gradually shifts away from the heavy-hole band (see Figure 3). As a result, only the light-hole band contributes to the Seebeck coefficient.
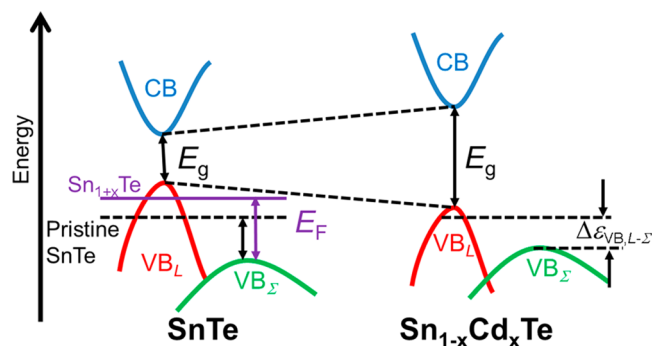

Figure 3. Schematic energy diagram of the electronic structure of SnTe near the Fermi level (E_F). E_g is the bandgap. The relative positions of the conduction band, light hole valence band (VB$_L$), and heavy hole valence (VB$_\Sigma$) bands are shown for pristine SnTe, Sn-compensated $Sn_{1+x}Te$, and $Sn_{1-x}Cd_xTe$.

Interestingly, we find that the $Sn_{1+x}Te$ samples with lower Seebeck coefficients at lower temperature have higher Seebeck coefficients when temperature is above 580 K (we call it a critical temperature here) (Figure 2b). The faster rise of the Seebeck coefficient at $T > 500$ K is reminiscent of the similar but more pronounced behavior of p-type PbTe, which is

attributed to the increasing contribution of the heavy hole Σ band at rising temperatures due to the thermal excitations. Considering the similarity of both crystal structure and electronic structure between PbTe and SnTe,[38,40,55−57] we deduce that the heavy hole band contribution is present in the high temperature properties of SnTe but is better manifested once a significant number of Sn vacancies has been removed. Support for this comes from the Hall coefficient (R_H) vs temperature (T) plot, where we find two peaks (∼523 K and ∼723 K), as shown in Figure 4. It is worth noting that the
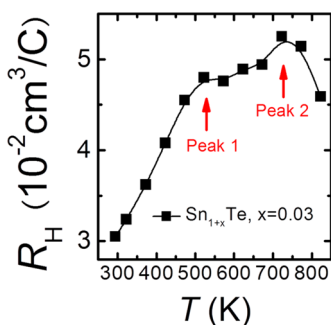
Figure 4. Hall coefficient as a function of temperature for a $Sn_{1+x}Te$ sample with $x = 0.03$.

temperature corresponding to the first peak (∼523 K) in the $R_H−T$ plot is similar to the critical temperature (∼580 K) observed in the $S−T$ plot (Figure 2b). The first peak in the $R_H−T$ plot is probably associated with onset of the contribution of the Σ band. The second peak in the $R_H−T$ plot is believed to be related to the onset of bipolar diffusion of carriers,[58] although no evidence of intrinsic excitation of electron transport can be observed. This discrepancy has also been observed in other lead chalcogenides and p-type skutterudites.[59−63] At 823 K, the Seebeck coefficient for the $x = 0.06$ sample is ∼150 μV/K, a 50% improvement over pristine SnTe.

Figure 2c depicts the power factors for all $Sn_{1+x}Te$ samples. The pristine SnTe has relatively high power factors (∼14 μW cm^{-1} K^{-2} at 300 K and ∼19 μW cm^{-1} K^{-2} at 823 K) in the entire temperature range, mainly benefiting from its very high electrical conductivity. The power factors deteriorate upon Sn-compensation in the low temperature range ($T < 650$ K) due to the simultaneously decreased electrical conductivities and Seebeck coefficients, but above 600 K, there is a greatly enhanced Seebeck coefficient for the Sn-compensated samples and the power factors improve with respect to SnTe itself.

The temperature dependent total thermal conductivity values for $Sn_{1+x}Te$ decrease monotonically with increasing x value (Figure 2d). The total thermal conductivity κ_{tot} is essentially a combination of two parts: the electronic contribution κ_{el} and the lattice contribution κ_{lat}. The electronic contribution can be evaluated by the Wiedemann−Franz relation $\kappa_{el} = L\sigma T$, where L is the Lorenz number, σ is the electrical conductivity, and T is the absolute temperature. In this study, the L value was obtained from the accepted approach of fitting the Seebeck data to the reduced chemical potential,[64−66] and the details can be found in Supporting Information. The lattice thermal conductivity κ_{lat} is then calculated by subtracting κ_{el} from κ_{tot}, and the results are shown in Figure 2e. There is no definite dependence between κ_{lat} and x, which suggests that the variation of Sn content in SnTe hardly affects the phonon transport. The lattice thermal conductivity is ∼2.2 W m^{-1} K^{-1}

at room temperature and ∼1 W m^{-1} K^{-1} at 823 K for SnTe, and it is comparable to undoped PbTe and PbSe,[15,67−69] indicating that SnTe has the potential of being a promising thermoelectric material if its properties could be better controlled. The ZTs as a function of temperature for all the $Sn_{1+x}Te$ compounds are shown in Figure 2f. The $x = 0.03$ sample shows a maximum ZT of ∼0.6 at 823 K, which is ∼50% improvement over the pristine SnTe because of the increased Seebeck coefficient as well as decreased total thermal conductivity. The above results demonstrate that Sn self-compensation is effective in suppressing the excessive hole concentration of SnTe.

2. Tuning the Band Structure of SnTe via Cd Alloying. Previous calculations indicated that the optimum band gaps for a good thermoelectric material should always be greater than $6k_BT$ (where k_B is Boltzmann constant, and T is the operation temperature), but can be much larger depending on the specific mechanism of electron scattering.[70] This simple rule of thumb implies that an ideal thermoelectric material operating around 800 K should have a band gap of at least ∼0.3 eV. This, however, is much larger than that of SnTe (∼0.18 eV at room temperature).[42] Even if we take into account that the energy gap of SnTe increases with rising temperature, similar to PbTe (∼4.2 × 10^{-4} eV/K),[71,72] at high temperature it will still only be ∼0.27 eV, smaller than the optimum value. Besides, even though we demonstrated above that Sn self-compensation is an effective way of reducing the hole density of SnTe, the resultant hole concentration is still very high, giving rise to a lower than desired Seebeck coefficient as well as a high electronic thermal conductivity. It is therefore essential to further decrease the hole concentration to more optimal levels with the aim of further enhancing the thermoelectric performance.

As discussed above, another concern is the large energy separation (∼0.3−0.4 eV at room temperature) between the light-hole band and heavy-hole band in SnTe.[38,40] Once the hole concentration is sufficiently low, the Fermi level will rise, moving away from the heavy-hole band (see Figure 3). Thus, the suppressed contribution from the heavy-hole band leads to a lower Seebeck coefficient at high temperature. In addition, considerable bipolar diffusion will occur in compounds with low carrier concentration if the band gap is not large enough, which will significantly deteriorate the high temperature performance.

We show here that these challenges can be overcome through the modification of the band structure, namely, widening the band gap and reducing the energy separation between the light-hole band and heavy-hole band. For the first time, using theory as a predictive guide to modify the electronic structure (described in a later section) we verify by experiment that both an increase in band gap and a significant decrease in energy separation between the light-hole band and heavy-hole band can be achieved in SnTe via alloying with the isovalent Cd atoms. Forming $Sn_{1−x}Cd_xTe$ has a profound impact on the electronic structure, and this is reflected in the measured charge properties and large enhancement in thermoelectric performance. This result opens a path to improving ZT.

Phase Compositions and Thermoelectric Transport Properties. Figure 5a shows the powder XRD patterns of SPSed $Sn_{1.03−x}Cd_xTe$ ($x = 0$, 0.01, 0.02, 0.03, 0.04, 0.05, and 0.06) samples. All patterns display single phase without noticeable impurities within our detection limit. The lattice parameter increases nearly linearly with increasing x up to 0.03, and beyond this value, it stays constant, suggesting that the
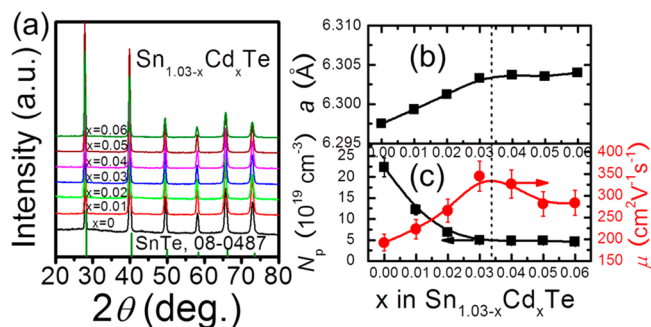
Figure 5. (a) Powder XRD patterns of $Sn_{1.03-x}Cd_xTe$ ($x = 0-0.06$) samples, (b) lattice parameters, and (c) carrier density and mobility as a function of x at room temperature. Inset of (a) standard diffraction patterns of SnTe (JCPDS Card 08−0487).

solubility limit of Cd in SnTe is around ∼0.03 near room temperature (Figure 5b). The lattice expansion of the Cd-doped samples is consistent with the larger radius of Cd^{2+} ions (∼0.97 Å) than that of Sn^{2+} ions (∼0.93 Å) and also demonstrates that Cd atoms have successfully substituted Sn atoms. The room temperature carrier concentrations (N_p) and mobilities (μ) of the samples are shown in Figure 5c. It can be seen that the hole density decreases gradually with increasing x until 0.03 and then remains almost unchanged. The hole mobility first increases with increasing x, reaching the peak value at $x = 0.03$, and then slightly deteriorates. The increase of carrier mobility upon Cd doping ($x \leq 0.03$) is possibly due to the diminished scattering arising from the significantly reduced hole population. However, for $x > 0.03$, the mobility is slightly reduced probably because of the emergence of an impurity phase, as Cd exceeds the solubility limit. It is surprising that Cd, although nominally isoelectronic with Sn, actually appears to act as an electron donor. The reason for this may be a decrease in the tendency of Sn to create vacancies in the presence of Cd alloying. The validity of this idea will have to be confirmed with future in-depth theoretical and experimental studies.

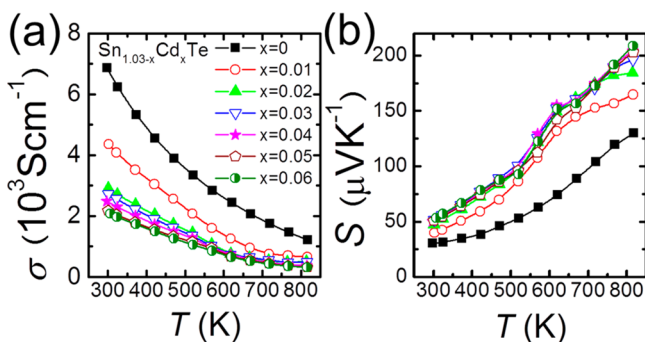The electrical transport properties of $Sn_{1.03-x}Cd_xTe$ ($x = 0-0.06$) samples are shown in Figure 6. The electrical conductivity

Figure 6. Electrical properties as a function of temperature for $Sn_{1.03-x}Cd_xTe$: (a) electrical conductivity; (b) Seebeck coefficient.

decreases with increasing temperature for all samples, showing typical degenerate semiconductor behavior. With increasing Cd content, the electrical conductivity decreases because of the decreased carrier concentration N_p ($x \leq 0.03$). The Seebeck coefficient increases with rising temperature up to 823 K without showing evidence of deterioration (Figure 6b). Furthermore, the Seebeck coefficient increases gradually with

decreasing N_p, which is different from the above-mentioned case of $Sn_{1+x}Te$.

The variation of Seebeck coefficient with hole concentration for pristine SnTe can be understood in light of a valence band model (VBM) which takes into account the nonparabolicity of the light-hole band.[38,40] The dotted line shown in the Pisarenko plot in Figure 7 shows the expected room temperature Seebeck
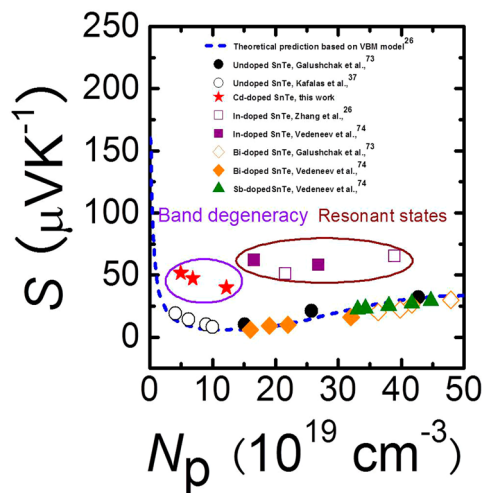

Figure 7. Room temperature Seebeck coefficient (S) as a function of carrier concentration (N_p) (Pisrenko plot). The dotted line is a theroretical prediction of the $S-N_p$ relationship based on a VBM model.

coefficient as a function of hole density dependent for SnTe based on the VBM model given by Zhang et al.[26] This model uses a light-hole band effective mass of ∼0.168 m_e, a heavy-hole band effective mass of ∼1.92 m_e, and an energy gap between the two valence bands of 0.35 eV, respectively. The room temperature Seebeck coefficients as a function of hole concentration for the $Sn_{1.03-x}Cd_xTe$ samples in our study are shown in Figure 7 (Pisarenko plot). Some previous data of In-,[26,73] Bi-,[73,74] Sb-,[74] and undoped[37,73] SnTe samples are also included for comparison. It can be seen that these SnTe samples (except In-doped) agree well with the VBM model, indicative of conventional doping behavior. The In-doped SnTe samples show a much higher Seebeck coefficient than the theoretical prediction, which is claimed to arise from resonant impurity states near the Fermi level induced by the In dopants.[26] We find that the Cd-doped SnTe samples also display markedly larger Seebeck coefficients than indicated by the Pisarenko plot calculation. We will discuss this issue later from an electronic band structure perspective.

Figure 8a plots the power factors as a function of temperature for $Sn_{1.03-x}Cd_xTe$ ($x = 0-0.06$) samples. It can be seen that, with respect to $Sn_{1.03}Te$, the power factors of Cd-doped samples are greatly enhanced at $T < 600$ K because of the enhanced Seebeck coefficient.

The temperature dependent total and lattice thermal conductivities for $Sn_{1.03-x}Cd_xTe$ are depicted in Figures 8b and c, respectively. The total thermal conductivity decreases with increasing Cd content until $x = 0.03$ and then remains unchanged. The lattice thermal conductivity is decreased relative to the $Sn_{1.03}Te$ sample and decreases further with increasing Cd content, presumably because of increased point defect scattering, and approaches ∼0.89 W/mK at 575 K for $x = 0.03$. At elevated temperature, however, it is only slightly
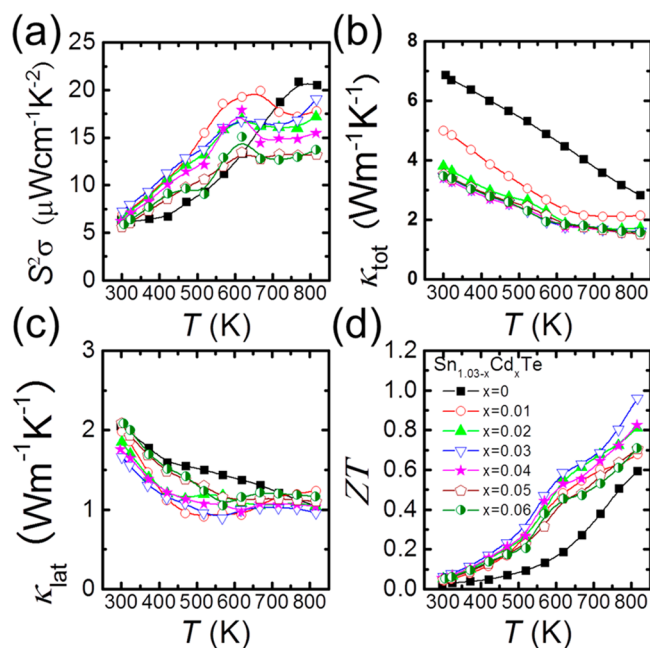
Figure 8. Thermoelectric properties as a function of temperature for $Sn_{1.03-x}Cd_xTe$: (a) power factor; (b) total thermal conductivity; (c) lattice thermal conductivity; (d) ZT.

Figure 9. Band structures of $Sn_{27}Te_{27}$, $Sn_{26}Cd_1Te_{27}$, and $Sn_{25}Cd_2Te_{27}$ as functions of (a) wavevector along the path $L \rightarrow \Sigma \rightarrow K$ in the rock-salt supercell BZ and (b) Cd concentration. In (a) the valence and conduction bands of pristine SnTe are shown as solid red lines; the valence, conduction, and Cd-defect bands of $Sn_{26}Cd_1Te_{27}$ are shown as solid black lines; and the valence, conduction, and Cd-defect bands of $Sn_{25}Cd_2Te_{27}$ are shown as dashed blue lines. The band structures for four different arrangements of 2 Cd atoms on the Sn lattice of SnTe are shown, with each structure giving rise to 2 Cd defect bands. In (b) the valence band at Σ (blue), valence band at L (black), conduction band at L (red), and Cd defect band (green) are shown as functions of Cd concentration in the SnTe supercell. For the Cd defect band and $x_{cd} = 0.74$ band structures, the bands are averaged over the BZ and each Cd–Cd configuration, respectively, with vertical bars indicating the standard deviation of each average. All energies are shown relative to the valence band maximum (VBM) of pristine SnTe. Cd substitution for Sn decreases the difference in energy between the valence bands of SnTe at the L and Σ points of the BZ primarily by opening the band gap, forming a Cd-defect band near the conduction band, and lowering the valence band at L.

lower with respect to $Sn_{1.03}Te$. Thus, by virtue of the enhanced Seebeck coefficient, the figure of merit is markedly enhanced by the incorporation of Cd, reaching ~0.96 at 823 K for $Sn_{1.03-x}Cd_xTe$ ($x = 0.03$), a ~60% improvement over the $Sn_{1.03}Te$ sample (Figure 8d).

Electronic Structure Calculations. To understand the origin of the Seebeck enhancement, we carried out density functional theory calculations of the electronic structures of both pristine SnTe and Cd-doped SnTe, as shown in Figure 9a. It can be clearly seen that the band gap is significantly increased by Cd alloying. We could not directly measure the band gaps of our SnTe-based materials by the conventional optical diffuse reflectance technique because of strong interference from the free carriers.[75] Nevertheless, the continuously increasing Seebeck coefficient with increasing temperature in the Cd-doped samples compared to the Seebeck maxima seen in $Sn_{1.03}Te$ (onset of bipolar effects) is consistent with a larger band gap upon Cd addition. In general, the band gap is related to the Seebeck coefficient by the Goldsmid relation $E_g \sim 2eS_{max}T_{max}$.[76] However, if the larger band gap is correct, one may be confused by the observation that the Cd-doped samples seem to have lower onset temperatures of bipolar diffusion with respect to the undoped one, Figure 8c. The reason for this is the lower hole density of these samples which raises the Fermi energy mitigating the effect of bandgap opening. Bipolar conduction is related not only to the band gap, but also with the carrier density. To make this point more clear, we need to compare the thermoelectric transport properties between cadmium doped and iodine doped SnTe-based compounds with similar hole densities at room temperature (see Figure S3, S4, and related discussion part in Supporting Information). There, one can more clearly see how Cd alloying in SnTe modifies the band structure (opening the band gap and diminishing the energy separation between the light-hole band and heavy-hole band).
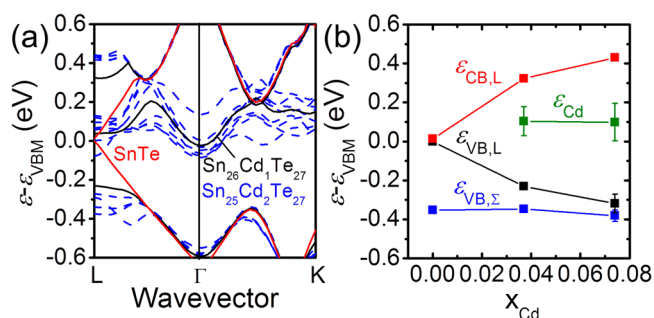
Another prominent feature in the electronic structure of $Sn_{1-x}Cd_xTe$ is the remarkable decrease in energy separation between the light-hole band heavy-hole band by Cd doping. This separation decreases from ~0.35 eV in pristine SnTe to only ~0.12 eV in 3 mol % Cd-doped SnTe. The Cd content dependent band gaps and energy separations are shown in Figure 9b for concentrations ranging from 0% (pristine SnTe) to 8% Cd substitution for SnTe. With increasing Cd fraction, the light-hole valence band and conduction band diverge quickly in energy, leading to an increase in band gap. In contrast, the heavy-hole valence band stays relatively constant in energy. Therefore, with the incorporation of Cd in the structure the light-hole valence band and heavy-hole band come closer together approaching band degeneracy. Similar band modifications have been found in Cd- and Mg-doped PbTe,[19,62] but this is the first time this type of valence band tuning is observed in SnTe. This increased valence band degeneracy leads to an enhancement of the Seebeck coefficient at high temperature because two bands are contributing to transport.

3. Nanostructuring with CdS/ZnS. Given the aforementioned demonstration of band structure tuning with Cd alloying in SnTe, we proceeded to introduce nanostructuring in this system to significantly reduce the lattice thermal conductivity. We selected CdS and ZnS as the second phases because previous studies in PbSe have shown limited solubility and a well-behaved nucleation and growth mechanism.[35] Further, any possible "alloying" behavior of these nanostructures in the matrix at high temperature will not only enlarge the band gap of the sample (suppressing any bipolar diffusion) but create more point defect lattice imperfections through incorporating more Cd or Zn atoms into the matrix, thus benefiting the high

7012

dx.doi.org/10.1021/ja500860m | *J. Am. Chem. Soc.* 2014, 136, 7006–7017

temperature thermoelectric performance. If the precipitates assume endotaxial (3-D coherent epitaxy) orientation with respect to the matrix, these CdS/ZnS nanostructures are likely to exert minimal influence on the carrier mobility and the Seebeck coefficient but can efficiently scatter phonons.

Figures 10a and 10b show the powder XRD patterns of sintered $SnCd_{0.03}Te$-x mol %CdS ($x = 0-5$) and $SnCd_{0.03}Te$-x
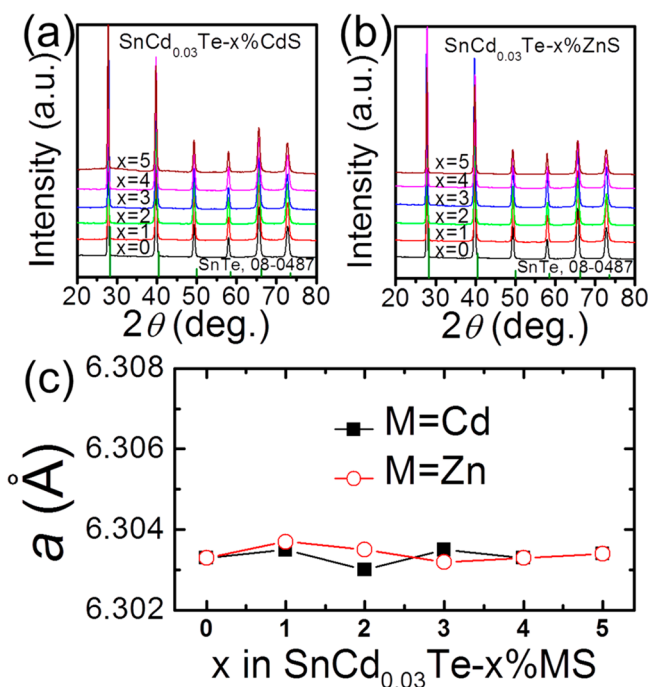

Figure 10. Powder XRD pattern of $SnCd_{0.03}Te$ nanostructuring with x mol % (a) CdS and (b) ZnS. (c) Room temperature lattice parameter as a function of x for these samples.

mol %ZnS ($x = 0-5$) materials, respectively. All samples appear as pure phase SnTe-based compounds with rock-salt structure with no detectable second phase. Figure 10c shows that the lattice parameters are nearly independent of the second phase content, indicating that the solubility of CdS/ZnS in the SnTe matrix is very low at room temperature.

The crystallographic, structural, and microanalytical analyses of the samples were carried out by conventional and high-resolution transmission electron microscopy (cTEM and HRTEM, respectively) as well as energy dispersive spectroscopy (EDS). In Figure 11a, a low magnification TEM image of $SnCd_{0.03}Te$-2%CdS sample shows high-density nanoprecipitates with dark contrast. Two orthogonal symmetry variants of the precipitates with elliptical shape are apparent in the image (the third being within the plan of the sample), and are shown schematically in the inset. The precipitates are oriented along the principal axes with respect to the matrix. The selected area diffraction (SAD) pattern along [001] orientation with an aperture that captures both the matrix and the precipitates shows only one set of Bragg reflection spots. This indicates that there is no distinguishable difference between the matrix and the precipitate lattice spacings, owing to their small lattice mismatch. An HRTEM image in Figure 11b depicts a coherent nanoscale precipitate (circled with dashed white line) embedded in the matrix. No line defects or discontinuities are observed at the matrix/precipitate interface, confirming coherently strained nanoscale endotaxial precipitates. The
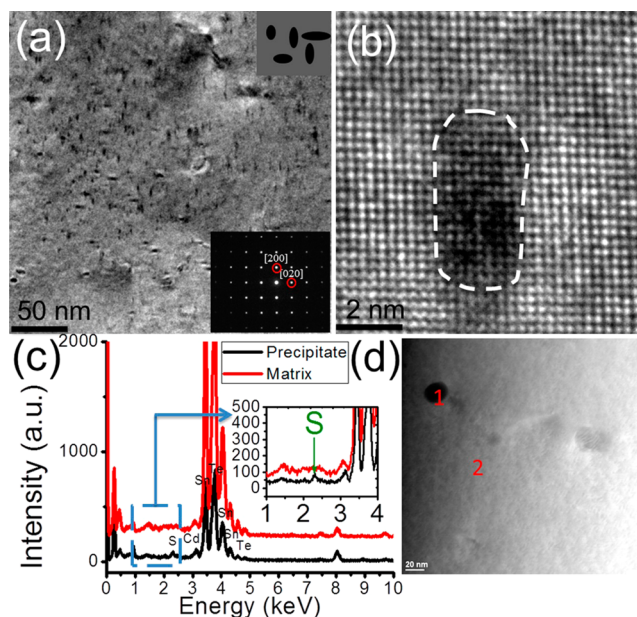

Figure 11. S/TEM and EDX analysis of $SnCd_{0.03}Te$-2%CdS. Low magnification TEM image in (a) shows the two obvious orthogonal variants (3rd variant being within the plane) of the nanoscale elongated precipitates, with the long axes along ⟨001⟩. The inset of the upper right corner of (a) schematically shows the two variants of the precipitates (dark color) embedded in the matrix (gray). The inset of the lower right corner of (a) is the SAD pattern taken along the [001] direction, depicting endotaxy between matrix and the precipitates. (b) HRTEM image of one nanoscale precipitate highlighted by the dashed white line. (c) is EDS of the $SnCd_{0.03}Te$-2%CdS sample and the corresponding STEM image as shown in (d). The spectra were taken at the precipitate and the matrix, respectively (spot 1 and spot 2). The Sn, Te, Cd, and S peaks were detected at the precipitate as shown in the inset. The matrix is with Sn, Te, and a little bit of Cd.

STEM-EDS results in Figure 11c indicate that the nanoscale precipitates are rich in Cd and S (spot 1 in Figure 11d), but the matrix (spot 2 shown in Figure 11d) is devoid of sulfur. Accurate quantitative composition analysis by EDS on the nanoprecipitates is challenging, because both the matrix and precipitates contribute to the EDS signals given considerable overlap between precipitate and matrix at such nanoscale form of the precipitates. Similar to the element distribution in $SnCd_{0.03}Te$-2%CdS, STEM EDS analysis of $SnCd_{0.03}Te$-2%ZnS sample confirms that zinc and sulfur are only found in the nanoscale precipitates, but not in the matrix, as shown in the Supporting Information.

We have also employed statistical analysis to obtain the size distribution of $SnCd_{0.03}Te$-2%CdS and $SnCd_{0.03}Te$-2%ZnS samples along the [001] orientation. Representative areas with similar fields of view used for the analysis are shown in the low-magnification TEM images in Figure 12a and b, respectively. In Figure 12c, the histograms of these two samples show notable difference. We find that for $SnCd_{0.03}Te$-2%CdS, most nanoscale precipitates range in size from 3 to 4 nm, but for $SnCd_{0.03}Te$-2%ZnS, the majority of precipitate size falls within the 4.5 to 7 nm range. The larger size ZnS nanostructures present a lower interface area to the matrix than CdS, which in relative terms may result in reduced phonon scattering.

The thermoelectric properties of the $SnCd_{0.03}Te$-x%CdS ($x = 0-5$) and $SnCd_{0.03}Te$-x%ZnS ($x = 0-5$) samples are

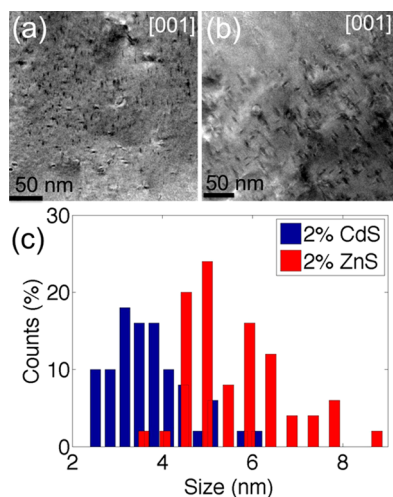**Figure 12.** Nanoscale precipitates distribution. (a) and (b) are areas used to analyze precipitate size for $SnCd_{0.03}Te$-2%CdS and $SnCd_{0.03}Te$-2%ZnS, respectively. Both of the images are along the [001] direction. (c) is the histograms of precipitate size for $SnCd_{0.03}Te$-2%CdS (blue) and $SnCd_{0.03}Te$-2%ZnS (red), respectively.

depicted in Figures 13 and 14, respectively. Generally, the electrical conductivity decreases with increasing CdS or ZnS content, whereas the Seebeck coefficient is insensitive to the second phase. The room temperature Hall measurement results are summarized in Table 1 and indicate that the introduction of CdS/ZnS second phases hardly affects the hole concentration but slightly deteriorates the mobility, likely because of increased interface scattering of holes. The invariance of hole densities further confirms that these second phases are immiscible with the matrix.

It is important to note that the electrical conductivity of the $SnCd_{0.03}Te$ sample shows a turnover at ~773 K attributed to some bipolar contribution, while those of the CdS- and ZnS-containing samples display turnover up at 823 K. This could be explained if at high temperature some Cd/Zn atoms dissolve into the matrix creating solid solution alloying which, as discussed above, enlarges the band gaps. In fact, this effect is manifested in the high temperature Hall measurements discussed below.

Figure 15a shows the high temperature (300−823 K) Hall coefficient R_H (up) and carrier mobilities μ (down) for $SnCd_{0.03}Te$, $SnCd_{0.03}Te$-2%CdS, and $SnCd_{0.03}Te$-2%ZnS. Similar to $Sn_{1.03}Te$, the R_H−T plots for $SnCd_{0.03}Te$, $SnCd_{0.03}Te$-2%CdS, and $SnCd_{0.03}Te$-2%ZnS samples also have two peaks. The first peak occurs at ~423 K, and is attributable to the onset of the contribution of the Σ band. The second peak is related to the bipolar diffusion, although we do not observe any evidence of decrease of Seebeck coefficient up to ~823 K (Figures 13b and 14b). As mentioned above, this discrepancy seems to be common in p-type lead chalcogenides and p-type skutterudites with complex valence band structures.[59−63] The temperatures corresponding to the second peak in the R_H−T plots vary with composition. Specifically, they are 623, 673, and 723 K for $SnCd_{0.03}Te$, $SnCd_{0.03}Te$-2%CdS, and $SnCd_{0.03}Te$-2%ZnS, respectively. The increase of the temperature corresponding to the onset of bipolar diffusion in the CdS- and ZnS-containing samples suggests that some Cd or Zn from CdS or ZnS likely dissolve into the matrix at elevated temperature, thus further opening the band gap of the SnTe matrix. This is also consistent with the trend of S−T plots shown in Figures 13b and 14b, where the $SnCd_{0.03}Te$ shows a topping of the Seebeck coefficient at ~823 K while in the 2%CdS/ZnS nanostructured samples the maximum occurs around 873 K. A temperature dependent solubility of Cd has been manifested in the PbTe-CdTe systems.[62] The carrier mobilities of the nanostructured samples are slightly deteriorated with respect to $SnCd_{0.03}Te$ itself, as shown in Figure 15a, because of the intensified interface scattering.

The overall power factors, as shown in Figures 13c and 14c, decrease gradually with increasing CdS/ZnS content because of the slightly lower electrical conductivity. The temperature
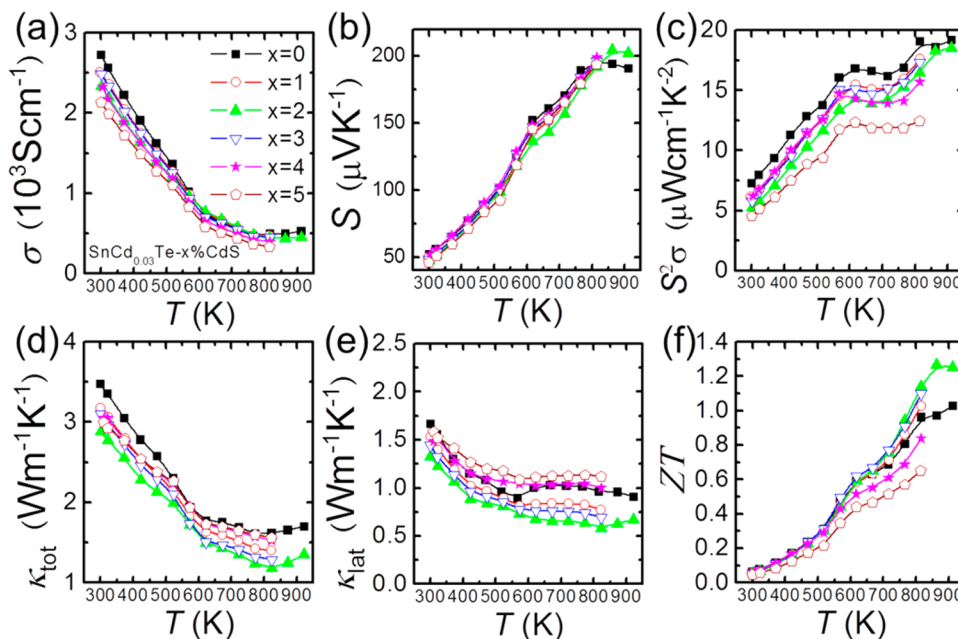

Figure 13. Thermoelectric properties as a function of temperature for $SnCd_{0.03}Te$ with different CdS content: (a) electrical conductivity; (b) Seebeck coefficient; (c) power factor; (d) total thermal conductivity; (e) lattice thermal conductivity; (f) ZT.

Figure 14. Thermoelectric properties as a function of temperature for $SnCd_{0.03}Te$ with different ZnS content: (a) electrical conductivity; (b) Seebeck coefficient; (c) power factor; (d) total thermal conductivity; (e) lattice thermal conductivity; (f) ZT.
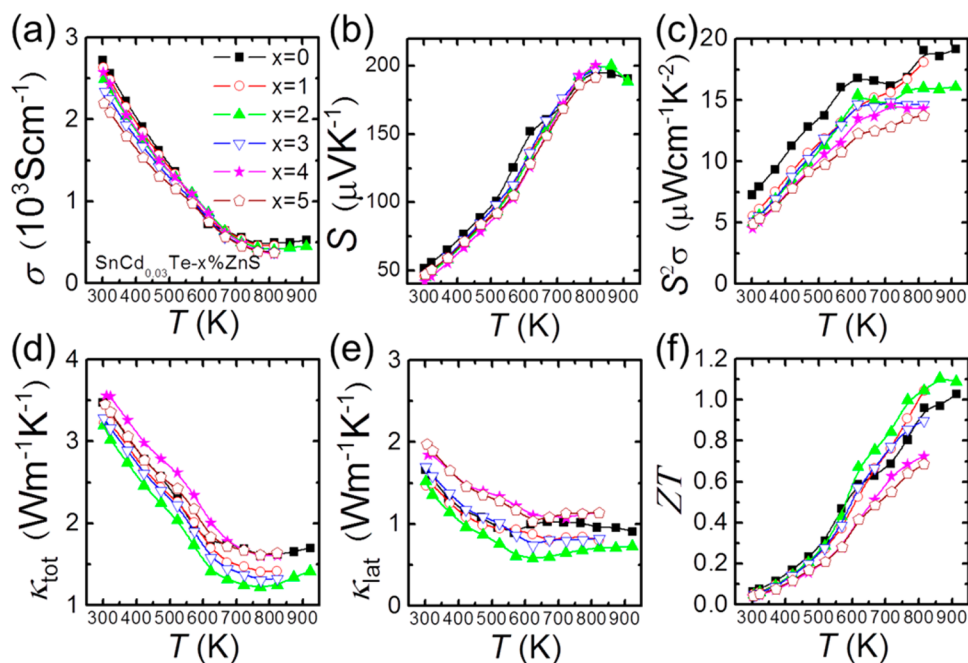
Table 1. Room Temperature Electrical Conductivity (σ), Hall Coefficient (R_H), Carrier Concentration (N_p), and Mobility (μ) Data for $SnCd_{0.03}Te$, $SnCd_{0.03}Te$-x mol %CdS, and $SnCd_{0.03}Te$-x mol %ZnS

Compositions	σ (10^3 S/cm)	R_H (10^{-7} m^3/C)	N_p (10^{19} cm^{-3})	μ (cm^2 V^{-1} s^{-1})
SnTe	7.8	0.13	47	104
$Sn_{1.03}Te$	6.8	0.27	23	184
$SnCd_{0.03}Te$	2.7	1.27	4.94	344
$SnCd_{0.03}Te$-1% CdS	2.5	1.31	4.76	329
$SnCd_{0.03}Te$-2% CdS	2.3	1.29	4.86	300
$SnCd_{0.03}Te$-3% CdS	2.5	1.12	5.60	278
$SnCd_{0.03}Te$-4% CdS	2.3	1.14	5.49	265
$SnCd_{0.03}Te$-5% CdS	2.1	1.11	5.63	237
$SnCd_{0.03}Te$-1% ZnS	2.6	1.28	4.90	336
$SnCd_{0.03}Te$-2% ZnS	2.5	1.24	5.04	310
$SnCd_{0.03}Te$-3% ZnS	2.3	1.24	5.05	290
$SnCd_{0.03}Te$-4% ZnS	2.6	1.17	5.34	302
$SnCd_{0.03}Te$-5% ZnS	2.2	1.25	5.01	275

Figure 15. (a) Temperature dependent Hall coefficient and mobility for three selected samples: $SnCd_{0.03}Te$, $SnCd_{0.03}Te$-2%CdS, and $SnCd_{0.03}Te$-2%ZnS; (b) lattice thermal conductivity as a function of x for $SnCd_{0.03}Te$-x mol % MS (M = Cd, Zn) at 300 and 823 K.

dependent total thermal conductivities are shown in Figures 13d and 14d for CdS- and ZnS-containing systems, respectively. It is apparent that in both cases, the total thermal conductivities generally decrease with increasing fraction of the second phase. The lattice thermal conductivities are shown in Figures 13e and 14e for the CdS and ZnS systems, respectively. The lattice thermal conductivities of the CdS-containing samples decrease with increasing temperature while those of ZnS-containing samples first decrease rapidly up to ~600 K and
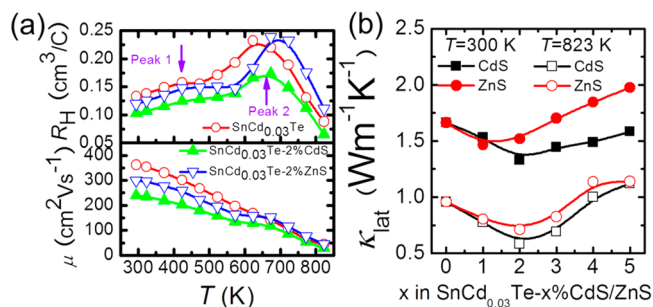
then remain nearly constant. Regardless of the temperature, the lattice thermal conductivity first decreases and then increases gradually with increasing CdS/ZnS content, approaching the minimum values of 0.58 W m^{-1} K^{-1} at $x = 2$, as shown in Figure 15b. This indicates that there is an optimal volume fraction of second phase for the strongest phonon scattering.[77] Moreover, the lattice thermal conductivities of the CdS-containing samples are slightly lower than those of ZnS-containing ones for the same x value. This may be a consequence of the different sizes (and number densities) of nanoprecipitates occurring in the matrix, as described above.

The temperature dependent ZT values of these systems are shown in Figures 13f and 14f. Clearly, the thermoelectric performance is further enhanced by the CdS/ZnS additives. The maximum ZTs reach ~1.3 and ~1.1 at 873 K for $SnCd_{0.03}Te$-2%CdS and $SnCd_{0.03}Te$-2%ZnS, respectively, which are larger than those of $Sn_{1-x}In_xTe$ (ZT ~ 1.1, 873 K)[26] and $AgSn_xSbTe_{2+x}$ (ZT ~ 1.0, 710 K)[78] systems, and are also superior to some other well-known p-type compounds, like skutterudites,[34] Si−Ge alloys,[79] Mg_2Si-based compounds,[80] and half-Heusler alloys[81] (Figure 16). Multiple samples of
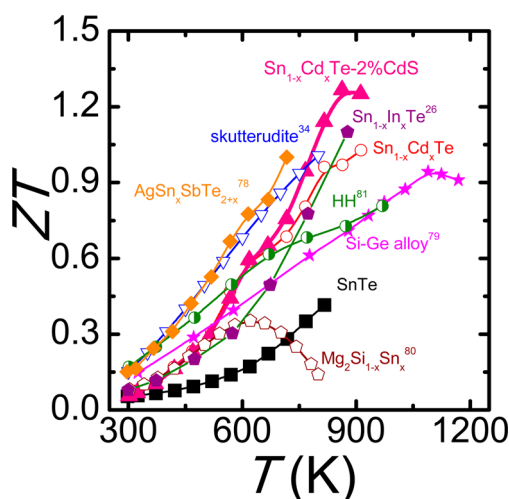
Figure 16. Comparison of ZT values among some best lead-free p-type thermoelectric materials working in the middle-to-high temperature range in this study and from available literatures.

$SnCd_{0.03}Te$-2%CdS were vacuum annealed at 723 K for 15 days and then the thermoelectric transport properties were rechecked. The results (see Supporting Information) indicate that electrical conductivity, Seebeck coefficient, and thermal conductivity of the unannealed and annealed samples were in agreement with previously prepared samples. This implies a high reproducibility and good thermal stability of this high performance thermoelectric material.

CONCLUDING REMARKS

SnTe can be transformed from a poor thermoelectric material to a high performing p-type lead-free system relevant to high temperature power generation by applying a synergistic band engineering and nanostructuring approach. Sn compensation in the SnTe lattice reduces the very high hole concentration and is a key prerequisite in optimizing the thermoelectric properties. A 3 mol % Sn self-compensation alone improves the ZT from 0.4 to 0.6 at 823 K. The alloying of Cd at Sn sites in the rock-salt structure even at only 3 mol % has very favorable effects on the band structure. As suggested by first-principles density functional theory calculations the modification of the electronic structure by Cd is significant and involves an increase of band gap and a decrease of the energy separation between the light-hole band at L and heavy-hole band at Σ points. This type of band engineering is a crucial finding of this work and is important in achieving a high figure of merit for this system of ~0.96 for $SnCd_{0.03}Te$. Finally, the use of endotaxial CdS/ZnS nanostructures further suppresses the lattice thermal conductivity of $Sn_{1-x}Cd_xTe$, leading to record ZT values of ~1.3 at 873 K. This is the highest ZT value reported for p-type SnTe-based thermoelectric materials. We observe stable and reproducible behavior of the high performance, and these results make SnTe superior to most leading p-type lead free thermoelectric materials. It is therefore an attractive alternative to lead chalcogenides for high temperature power generation applications.

ASSOCIATED CONTENT

Ⓢ Supporting Information

The summary of calculation method for Lorenz number ("Calculation of Lorenz number"); the discussion on bipolar diffusion and band degeneracy; thermal diffusivity, heat capacity, and calculated Lorenz number as a function of x for $Sn_{1+x}Te$ (Figure S1), $Sn_{1.03-x}Cd_xTe$ (Figure S2), $SnCd_{0.03}Te$-x%CdS (Figure S7), $SnCd_{0.03}Te$-x%ZnS (Figure S8); thermoelectric properties of $SnCd_{0.03}Te$-2%CdS samples of initially prepared, reproduced, and the reproduced one after vacuum annealing at 723 K for 15 days (Figure S9); room temperature Seebeck coefficient as a function of hole density for 0.5 mol % iodine doped SnTe (Figure S3); a comparison of thermoelectric transport properties between iodine doped and cadmium doped SnTe (Figure S4); detailed TEM microstructural and elemental analysis for $SnCd_{0.03}Te$-2%CdS (Figures S5) and $SnCd_{0.03}Te$-2%ZnS (Figures S6); densities of all samples investigated in this study (Table S1). This material is available free of charge via the Internet at http://pubs.acs.org.

AUTHOR INFORMATION

Corresponding Author
*E-mail: m-kanatzidis@northwestern.edu.

Notes
The authors declare no competing financial interest.

ACKNOWLEDGMENTS

REFERENCES

(1) Bell, L. E. *Science* **2008**, *321*, 1457.
(2) Heremans, J. P.; Dresselhaus, M. S.; Bell, L. E.; Morelli, D. T. *Nat. Nanotechnol.* **2013**, *8*, 471.
(3) Venkatasubramanian, R.; Siivola, E.; Colpitts, T.; O'quinn, B. *Nature* **2001**, *413*, 597.
(4) Bell, L. E.; Bartosh, S. M.; Davis, C. L.; Dobbels, F.; Al-Uzri, A.; Lotstein, D.; Reiss, J.; Dharnidharka, V. R.; Attendees, C. *Am. J. Transplant.* **2008**, *8*, 2230.
(5) Vining, C. B. *Nat. Mater.* **2009**, *8*, 83.
(6) Sales, B.; Mandrus, D.; Williams, R. K. *Science* **1996**, *272*, 1325.
(7) Hsu, K. F.; Loo, S.; Guo, F.; Chen, W.; Dyck, J. S.; Uher, C.; Hogan, T.; Polychroniadis, E. K.; Kanatzidis, M. G. *Science* **2004**, *303*, 818.
(8) Poudel, B.; Hao, Q.; Ma, Y.; Lan, Y.; Minnich, A.; Yu, B.; Yan, X.; Wang, D.; Muto, A.; Vashaee, D. *Science* **2008**, *320*, 634.
(9) DiSalvo, F. J. *Science* **1999**, *285*, 703.
(10) Sootsman, J. R.; Chung, D. Y.; Kanatzidis, M. G. *Angew. Chem., Int. Ed.* **2009**, *48*, 8616.
(11) (a) Kanatzidis, M. G. *Chem. Mater.* **2010**, *22*, 648. (b) Zhao, L.-D.; Dravid, V. P.; Kanatzidis, M. G. *Energy Environ. Sci.* **2014**, *7*, 251.
(12) Vineis, C. J.; Shakouri, A.; Majumdar, A.; Kanatzidis, M. G. *Adv. Mater.* **2010**, *22*, 3970.
(13) Heremans, J. P.; Jovovic, V.; Toberer, E. S.; Saramat, A.; Kurosaki, K.; Charoenphakdee, A.; Yamanaka, S.; Snyder, G. J. *Science* **2008**, *321*, 554.
(14) (a) Jaworski, C. M.; Kulbachinskii, V.; Heremans, J. P. *Phys. Rev. B* **2009**, *80*, 233201. (b) Bilc, D.; Mahanti, S. D.; Hsu, K. F.; Quarez, E.; Pcionek, R.; Kanatzidis, M. G. *Phys. Rev. Lett.* **2004**, *93*, 146403-1. (c) Ahn, K.; Han, M. K.; He, J. Q.; Androulakis, J.; Ballikaya, S.; Uher, C.; Dravid, V. P.; Kanatzidis, M. G. *J. Am. Chem. Soc.* **2010**, *132*, 5227. (d) Ahmad, S.; Mahanti, S. D.; Hoang, K.; Kanatzidis, M. G. *Phys. Rev. B* **2006**, *74*, 155205-1.

(15) Zhang, Q. Y.; Wang, H.; Liu, W. S.; Wang, H. Z.; Yu, B.; Zhang, Q.; Tian, Z. T.; Ni, G.; Lee, S.; Esfarjani, K.; Chen, G.; Ren, Z. F. *Energy Environ. Sci.* **2012**, *5*, 5246.

(16) Heremans, J. P.; Wiendlocha, B.; Chamoire, A. M. *Energy Environ. Sci.* **2012**, *5*, 5510.

(17) Pei, Y.; Shi, X.; LaLonde, A.; Wang, H.; Chen, L.; Snyder, G. J. *Nature* **2011**, *473*, 66.

(18) Liu, W.; Tan, X. J.; Yin, K.; Liu, H. J.; Tang, X. F.; Shi, J.; Zhang, Q. J.; Uher, C. *Phys. Rev. Lett.* **2012**, *108*, 166601.

(19) Zhao, L. D.; Wu, H. J.; Hao, S. Q.; Wu, C. I.; Zhou, X. Y.; Biswas, K.; He, J. Q.; Hogan, T. P.; Uher, C.; Wolverton, C.; Dravid, V. P.; Kanatzidis, M. G. *Energy Environ. Sci.* **2013**, *6*, 3346.

(20) Yang, J.; Meisner, G. P.; Chen, L. *Appl. Phys. Lett.* **2004**, *85*, 1140.

(21) Abeles, B. *Phys. Rev.* **1963**, *131*, 1906.

(22) Zeier, W. G.; Pei, Y. Z.; Pomrehn, G.; Day, T.; Heinz, N.; Heinrich, C. P.; Snyder, G. J.; Tremel, W. *J. Am. Chem. Soc.* **2013**, *135*, 726.

(23) Tan, G.; Liu, W.; Chi, H.; Su, X.; Wang, S.; Yan, Y.; Tang, X.; Wong-Ng, W.; Uher, C. *Acta Mater.* **2013**, *61*, 7693.

(24) Tan, G.; Wang, S.; Tang, X. *Sci. Adv. Mater.* **2013**, *5*, 1974.

(25) Minnich, A. J.; Dresselhaus, M. S.; Ren, Z. F.; Chen, G. *Energy Environ. Sci.* **2009**, *2*, 466.

(26) Zhang, Q.; Liao, B. L.; Lan, Y. C.; Lukas, K.; Liu, W. S.; Esfarjani, K.; Opeil, C.; Broido, D.; Chen, G.; Ren, Z. F. *Proc. Natl. Acad. Sci. U. S. A.* **2013**, *110*, 13261.

(27) Tan, G.; Liu, W.; Wang, S.; Yan, Y.; Li, H.; Tang, X.; Uher, C. *J. Mater. Chem. A* **2013**, *1*, 12657.

(28) Zhao, L. D.; Lo, S. H.; He, J.; Li, H.; Biswas, K.; Androulakis, J.; Wu, C. I.; Hogan, T. P.; Chung, D. Y.; Dravid, V. P.; Kanatzidis, M. G. *J. Am. Chem. Soc.* **2011**, *133*, 20476.

(29) Zhao, L. D.; He, J.; Wu, C. I.; Hogan, T. P.; Zhou, X.; Uher, C.; Dravid, V. P.; Kanatzidis, M. G. *J. Am. Chem. Soc.* **2012**, *134*, 7902.

(30) Zhao, L. D.; He, J.; Hao, S.; Wu, C. I.; Hogan, T. P.; Wolverton, C.; Dravid, V. P.; Kanatzidis, M. G. *J. Am. Chem. Soc.* **2012**, *134*, 16327.

(31) Lee, Y.; Lo, S. H.; Androulakis, J.; Wu, C. I.; Zhao, L. D.; Chung, D. Y.; Hogan, T. P.; Dravid, V. P.; Kanatzidis, M. G. *J. Am. Chem. Soc.* **2013**, *135*, 5152.

(32) Biswas, K.; He, J.; Zhang, Q.; Wang, G.; Uher, C.; Dravid, V. P.; Kanatzidis, M. G. *Nat. Chem.* **2011**, *3*, 160.

(33) Biswas, K.; He, J.; Blum, I. D.; Wu, C. I.; Hogan, T. P.; Seidman, D. N.; Dravid, V. P.; Kanatzidis, M. G. *Nature* **2012**, *489*, 414.

(34) Tan, G.; Zheng, Y.; Tang, X. *Appl. Phys. Lett.* **2013**, *103*, 183904.

(35) Zhao, L. D.; Hao, S. Q.; Lo, S. H.; Wu, C. I.; Zhou, X. Y.; Lee, Y.; Li, H.; Biswas, K.; Hogan, T. P.; Uher, C.; Wolverton, C.; Dravid, V. P.; Kanatzidis, M. G. *J. Am. Chem. Soc.* **2013**, *135*, 7364.

(36) Brebrick, R. F. *J. Phys. Chem. Solids* **1963**, *24*, 27.

(37) Kafalas, J. A.; Brebrick, R. F.; Strauss, A. J. *Appl. Phys. Lett.* **1964**, *4*, 93.

(38) Rogers, L. M. *J. Phys. D: Appl. Phys.* **1968**, *1*, 845.

(39) Singh, D. J. *Funct. Mater. Lett.* **2010**, *3*, 223.

(40) Brebrick, R.; Strauss, A. *Phys. Rev.* **1963**, *131*, 104.

(41) Esaki, L.; Stiles, P. J. *Phys. Rev. Lett.* **1966**, *16*, 1108.

(42) Dimmock, J. O.; Melngail, I.; Strauss, A. J. *Phys. Rev. Lett.* **1966**, *16*, 1193.

(43) Andrevv, A. *J. Phys. Colloq.* **1968**, *29*, C4.

(44) Voyles, P.; Grazul, J.; Muller, D. *Ultramicroscopy* **2003**, *96*, 251.

(45) Hohenberg, P.; Kohn, W. *Phys. Rev. B* **1964**, *136*, B864.

(46) Kohn, W.; Sham, L. J. *Phys. Rev.* **1965**, *140*, 1133.

(47) Kresse, G.; Furthmuller, J. *Phys. Rev. B* **1996**, *54*, 11169.

(48) Blochl, P. E. *Phys. Rev. B* **1994**, *50*, 17953.

(49) Perdew, J. P.; Burke, K.; Ernzerhof, M. *Phys. Rev. Lett.* **1996**, *77*, 3865.

(50) Saal, J. E.; Kirklin, S.; Aykol, M.; Meredig, B.; Wolverton, C. *JOM* **2013**, *65*, 1501.

(51) Lany, S.; Zunger, A. *Modell. Simul. Mater. Sci. Eng.* **2009**, *17*, 084002.

(52) Rogacheva, E. I. *J. Phys. Chem. Solids* **2008**, *69*, 259.

(53) Littlewood, P.; Mihaila, B.; Schulze, R.; Safarik, D.; Gubernatis, J.; Bostwick, A.; Rotenberg, E.; Opeil, C.; Durakiewicz, T.; Smith, J. *Phys. Rev. Lett.* **2010**, *105*, 086404.

(54) Jaworski, C. M.; Nielsen, M. D.; Wang, H.; Girard, S. N.; Cai, W.; Porter, W. D.; Kanatzidis, M. G.; Heremans, J. P. *Phys. Rev. B* **2013**, *87*, 045203.

(55) Tung, Y. W.; Cohen, M. L. *Phys. Rev.* **1969**, *180*, 823.

(56) Bernick, R. L.; Kleinman, L. *Solid State Commun.* **1970**, *8*, 569.

(57) Bauer Pereira, P.; Sergueev, I.; Gorsse, S.; Dadda, J.; Müller, E.; Hermann, R. P. *Phys. Status Solidi B* **2013**, *250*, 1300.

(58) Joffe, A. F. *Can. J. Phys.* **1956**, *34*, 1342.

(59) Wang, H.; Pei, Y.; LaLonde, A. D.; Snyder, G. J. *Adv. Mater.* **2011**, *23*, 1366.

(60) Pei, Y.; Wang, H.; Snyder, G. J. *Adv. Mater.* **2012**, *24*, 6125.

(61) Pei, Y.; Lensch-Falk, J.; Toberer, E. S.; Medlin, D. L.; Snyder, G. J. *Adv. Funct. Mater.* **2011**, *21*, 241.

(62) Pei, Y.; LaLonde, A. D.; Heinz, N. A.; Snyder, G. J. *Adv. Energy Mater.* **2012**, *2*, 670.

(63) Qiu, P. F.; Yang, J.; Liu, R. H.; Shi, X.; Huang, X. Y.; Snyder, G. J.; Zhang, W.; Chen, L. D. *J. Appl. Phys.* **2011**, *109*, 063713.

(64) Girard, S. N.; He, J.; Zhou, X.; Shoemaker, D.; Jaworski, C. M.; Uher, C.; Dravid, V. P.; Heremans, J. P.; Kanatzidis, M. G. *J. Am. Chem. Soc.* **2011**, *133*, 16588.

(65) Johnsen, S.; He, J.; Androulakis, J.; Dravid, V. P.; Todorov, I.; Chung, D. Y.; Kanatzidis, M. G. *J. Am. Chem. Soc.* **2011**, *133*, 3460.

(66) May, A. F.; Fleurial, J. P.; Snyder, G. J. *Phys. Rev. B* **2008**, *78*, 125205.

(67) Wang, H.; Schechtel, E.; Pei, Y.; Snyder, G. J. *Adv. Energy Mater.* **2013**, *3*, 488.

(68) Pei, Y.; LaLonde, A.; Iwanaga, S.; Snyder, G. J. *Energy Environ. Sci.* **2011**, *4*, 2085.

(69) Ahn, K.; Biswas, K.; He, J.; Chung, I.; David, V.; Kanatzidis, M. G. *Energy Environ. Sci.* **2013**, *6*, 1529.

(70) Sofo, J.; Mahan, G. *Phys. Rev. B* **1994**, *49*, 4565.

(71) Ahmad, S.; Mahanti, S. D. *Phys. Rev. B* **2010**, *81*, 165203.

(72) Bilc, D. I.; Mahanti, S. D.; Kanatzidis, M. G. *Phys. Rev. B* **2006**, *74*, 125202.

(73) Vedeneev, V. P.; Krivoruchko, S. P.; Sabo, E. P. *Semiconductors* **1998**, *32*, 241.

(74) Galushchak, M.; Freik, D.; Ivanyshyn, I.; Lisak, A.; Pyts, M. *J. Thermoelectr.* **2000**, *1*, 42.

(75) Zemel, J.; Jensen, J.; Schoolar, R. *Phys. Rev.* **1965**, *140*, A330.

(76) Goldsmid, H.; Sharp, J. *J. Electron. Mater.* **1999**, *28*, 869.

(77) Sootsman, J. R.; Pcionek, R. J.; Kong, H. J.; Uher, C.; Kanatzidis, M. G. *Chem. Mater.* **2006**, *18*, 4993.

(78) Han, M.-K.; Androulakis, J.; Kim, S.-J.; Kanatzidis, M. G. *Adv. Energy Mater.* **2012**, *2*, 157.

(79) Joshi, G.; Lee, H.; Lan, Y.; Wang, X.; Zhu, G.; Wang, D.; Gould, R. W.; Cuff, D. C.; Tang, M. Y.; Dresselhaus, M. S. *Nano Lett.* **2008**, *8*, 4670.

(80) Liu, W.; Yin, K.; Su, X.; Li, H.; Yan, Y.; Tang, X.; Uher, C. *Intermetallics* **2013**, *32*, 352.

(81) Yan, X.; Joshi, G.; Liu, W.; Lan, Y.; Wang, H.; Lee, S.; Simonson, J.; Poon, S.; Tritt, T.; Chen, G. *Nano Lett.* **2010**, *11*, 556.